ACS APPLIED MATERIALS & INTERFACES

RESEARCH ARTICLE

www.acsami.org

Interfacial Synthesis: Amphiphilic Monomers Assisted Ultrarefining of Mesoporous Manganese Oxide Nanoparticles and the Electrochemical Implications

Wei Xiao,[†,‡] Di Hu,[†] Chuang Peng,[†] and George Z. Chen*[,†]

[†]Department of Chemical and Environmental Engineering, and Energy and Sustainability Research Division, Faculty of Engineering, University of Nottingham, Nottingham NG7 2RD, United Kingdom

[‡]School of Resource and Environmental Science, Wuhan University, Wuhan, 430072, P. R. China

Supporting Information

ABSTRACT: Amphiphilic monomers, namely pyrrole and aniline, were used to reduce permanganate ion (MnO_4^-) at the dichloromethane/water interface for the preparation of ultrafine manganese oxide (MnO_x, $x \leq 2$) nanoparticles (NPs). These monomers did not undergo polymerization upon oxidation by MnO_4^-, but exerted an interesting effect of ultrarefining the produced MnO_x NPs from reducing MnO_4^- at the organoaqueous interface. This was attributed to the ability of the monomer to access the interfacial reaction sites from both organic and aqueous phases, and hence retard the as-produced MnO_x nuclei from aggregation at the interface. Such obtained products were mesoporous matrixes of three-dimensionally interconnected and uniform pseudospherical MnO_x NPs (<20 nm). On the contrary, using a more hydrophobic monomer, i.e., *o*-aminophenol, to reduce MnO_4^- produced a composite of nanobelts of poly(*o*-aminophenol) embedded in micrometer-sized MnO_x blocks. The ultrafine MnO_x NPs prepared from using aniline or pyrrole exhibited highly capacitive behavior in aqueous Na_2SO_4, promising their use in supercapacitors. It was also found that the MnO_x NPs prepared from pyrrole-assisted synthesis possessed higher specific capacitance than that from aniline-assisted synthesis, despite the latter having a higher specific surface area. This difference is discussed in terms of crystallographic properties and water contents of these two samples.

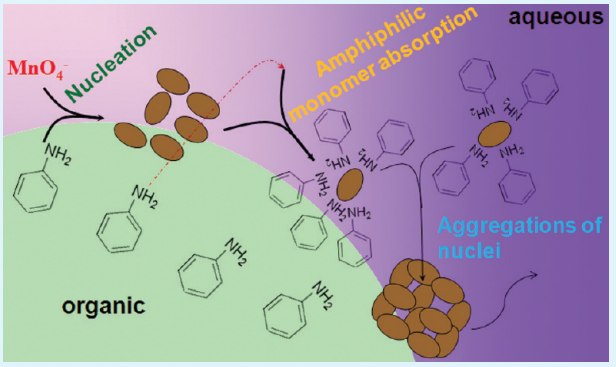

KEYWORDS: ultrafine nanoparticles, manganese oxides, amphiphilic monomer, interfacial synthesis, mesoporous materials, supercapacitors

1. INTRODUCTION

Manganese oxides (MnO_x, $x \leq 2$), particularly when functionalized via structure and surface refining, have been a focus of materials research for over a century to achieve desirable physicochemical properties for a wide range of applications.[1] They are rich in surface activities and electrochemistry, and often used as a "versatile" electrode material in various processes and devices, including electro-synthesis,[2] electrochromic devices,[3] alkaline primary batteries,[4] electrochemical sensors,[5,6] lithium ion batteries,[7−9] electrocatalysts,[10−12] and supercapacitors (SCs).[13−20] Among these, SCs present a unique combination of high power capability and reasonable energy capacity, and can complement other low power high capacity devices, e.g., lithium ion batteries and fuel cells, in provision of the energy storage solution for the so-called "smart-grid".[21] There are various materials investigated and used for SCs, but MnO_x are merited for their abundant resources, affordable production, and low environmental impact.[13,19,20]

Energy can be stored in MnO_x based SCs through either or both of (1) double layer capacitance (adsorption/desorption of ions at the electrode/electrolyte interface), and (2) pseudocapacitance (intercalation/deintercalation of cations into/from the oxide lattices with simultaneous redox reactions involving electron transfer in the conduction band).[13,19,20] Therefore, one of the strategies to enhance the performance of MnO_x electrodes is to introduce porous structures at nanoscales, which in turn increases the surface area for ion adsorption, and also shortens the transport paths of electrons and ions.[13,19,20,22] The main challenge to implement such a strategy comes from the yet limited number of synthetic routes for controlled synthesis of MnO_x in the form of nanoparticles (NPs) smaller than 20 nm that are well-dispersed and arranged into an ordered porous form. Apart from electrochemical synthesis,[23,24] wet-chemical bottom-up routes are presently most-fashionable on nanosynthesis of MnO_x, in which the product morphologies are mainly determined by the rate of nuclei growth (governing the formation of building blocks for desired structures) and the extent to which the building

Received: May 17, 2011
Accepted: July 27, 2011
Published: July 27, 2011

blocks aggregate or assemble. In addition, the aggregation process also plays an important role in tailoring the features of the porous structure in the product.

A widely applied wet-chemical approach is the hydrothermal synthesis that has been successfully used to produce various nanostructured MnO_x such as nanorods, nanotubes and nanosheets.[11,25−28] However, the high temperature and pressure presented in the hydrothermal reaction facilitate the Ostwald ripening process[29] of the generated nuclei or the assembly of building blocks to occur violently. The resulting anisotropic growth and assembly can lead to the formation of either MnO_x building blocks larger than 50 nm, or clusters in microscale hierarchical structures. It has also been reported that nano-MnO_x can be prepared *via* redox reactions between permanganates and organic reducing agents, in which the MnO_x building blocks are of particle sizes less than 20 nm.[30−34] For instance, mesoporous MnO_x with NP sizes in the range of 5−13 nm and of ca. 5 nm have been successfully prepared using ethylene glycol[32] and ascorbic acid[33] as the reducing agents, respectively. However, not all attempts involving the organic reducing agents achieved success. The MnO_x synthesized using fumaric acid were microscale granules evolving from the overagglomeration of smaller particles.[35] More recently, the organic/inorganic interfacial synthesis has been proposed and proven to be an effective method for the synthesis of mesoporous ultrathin MnO_x nanomterials.[9,36−40] However, the morphologies, crystallographic properties, and chemical compositions of the reported MnO_x prepared by the interfacial route are quite different, which provokes investigations on the relationship between synthetic parameters, product microstructures and properties.

Herein, we present a self-templating approach based on interfacial synthesis of mesoporous matrixes consisting of uniform MnO_x NPs with the diameters less than 20 nm. Specially, the important roles of amphiphlic monomers are highlighted in terms of their functions on determining the morphologies and components of the final products. The microstructures and electrochemical properties of the prepared ultrafine MnO_x NPs are investigated and analyzed to identify the possible correlation.

2. EXPERIMENTAL SECTION

All chemicals were of analytical grade from Sigma-Aldrich and used as received. In a typical interfacial synthesis experiment, 1 mL of monomer (aniline or pyrrole) was dissolved in 100 mL of dichloromethane (CH_2Cl_2) to form the organic phase. The aqueous phase was prepared via dissolving 0.2 g potassium permanganate ($KMnO_4$) in 100 mL of deionized water. Both solutions were cooled in a refrigerator to 4 °C. The aqueous solution was then poured onto the organic one. After violent shaking for 1 min and standing for 1 min, a static and well-defined organoaqueous interface appeared, as shown in Figure 1 (left photo). Such obtained two-phase bath was then placed in the refrigerator at 4 °C overnight. It should be noted that the precursory monomer was in excess to $KMnO_4$ in stoichiometry. After the reaction, the characteristic purple color of the permanganate ion totally disappeared as evidenced by Figure 1 (right photos), indicating full consumption of the permanganate. After pipetting the lower organic solution from the bath, a brown powder was sampled by centrifugating the remaining aqueous suspension. The powder was rinsed in deionized water for three times and ethanol once. The final product was collected after room-temperature vacuum-drying. In the following discussions, the prepared samples by using aniline and pyrrole as monomers are notated as An-MnO_x and Py-MnO_x, respectively. It is worth mentioning that without the violent shaking step, the reaction would produce larger and less uniform MnO_x

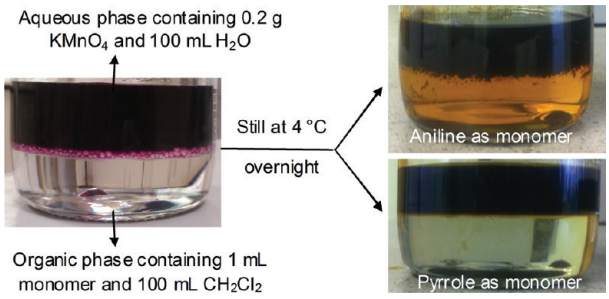

Figure 1. Optical photos of the interfacial reaction baths before (left) and after overnight standing in fridge at 4 °C (right).

NPs, see Figure S1 in the Supporting Information. Also, in the absence of the monomer, no MnO_x was produced.

For comparison, the coprecipitation synthesis was also carried out under the same conditions as those in the interfacial route except for changing CH_2Cl_2 to deionized water. In these experiments, 0.2 g *o*-aminophenol (*o*AP) and 0.6 g $KMnO_4$ (excess in stoichiometry) were also used as the feedstock.

Crystallographic information of all samples was investigated by powder X-ray diffraction (XRD; Shimadzu XRD-6000, Cu Kα, λ = 1.5406 Å) at a scanning rate of 2° min^{-1}. Morphologies of samples were examined by field-emission scanning electron microscopy (FESEM; Hitachi, S-4300), high-resolution transmission electron microscopy (HRTEM, JEOL 3010, 200 kV) and selected area electron diffraction (SAED). Elemental analysis was carried out using the CHNS-O Analyzer (Flash EA, 1112 Series, Thermo Electron Corporation) and energy dispersive spectroscopy (EDS, attached to the SEM). X-ray photoelectron spectroscopy (XPS) was performed on a Phobios 100 electron analyzer equipped with five channeltrons and a nonmonochromatized Mg Kα X-ray source (1253.6 eV). The C 1s peak at 285.0 eV due to adventitious carbon was used as an internal reference. Thermal behaviors of samples were examined by thermogravimetry and differential thermal analysis (TGA/DTA, Shimadzu DTG-60) from room temperature up to 700 °C at a heating ramp of 5 °C min^{-1} in air. The Brunauer−Emmett−Teller (BET) surface areas were determined by N_2 adsorption/desorption isotherm at 77 K (Micromeritics Tristar 3020). The pore-size distributions were calculated from the adsorption curve by the Barrett−Joyner−Halenda (BJH) method.

The working electrodes for electrochemical investigations were made by pressing the paste of mixed MnO_x (active material, 80 wt %), polyvinylidene difluoride (PVDF, binder, 10 wt %) and acetylene black (conductive agent, 10 wt %) on a 1 cm^2 Ni foil. The loadings of active materials were 1.50 and 1.41 mg cm^{-2} for the An-MnO_x and Py-MnO_x electrodes, respectively. All electrochemical measurements were carried out in a conventional three-electrode cell with a Pt foil (2 cm ×2 cm) counter, and the Ag/AgCl reference electrodes in the aqueous electrolyte of 1.0 mol L^{-1} Na_2SO_4. Cyclic voltammetry (CV) and galvanostatic charge/discharge (GCD) cycling were performed on a CHI electrochemical station. The electrochemical impedance spectra (EIS) were also investigated at the open-circuit potentials (0.25 V for An-MnO_x and 0.30 V for Py-MnO_x versus Ag/AgCl) in the frequency range of 10^5 to 0.02 Hz with an amplitude of 5 mV (Autolab PGSTAT30). The specific capacitance, C (F g^{-1}), was calculated from the following equation that is applicable to rectangular CVs or triangular GCD plots,

$$C = \frac{Q}{m\Delta E}$$

where Q (C) is the charge obtained by integration of the discharging current of the CV or the GCD plot, m (g) the mass of MnO_x, and ΔE (V) the potential window.

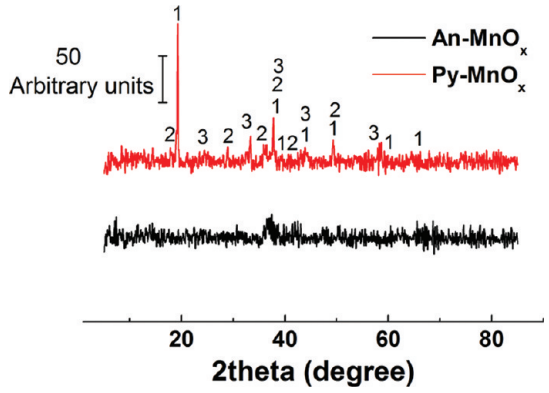

Figure 2. Powder XRD patterns of samples prepared by interfacial synthesis. "1" denotes λ-MnO_2 (JCPDS No. 44−0992, cubic, *Fd*3*m*, $a = b = c = 8.03$ Å); "2" represents α-MnO_2 (JCPDS No. 44−0141, tetragonal, *I*4/*m*, $a = b = 9.78$ Å, $c = 2.86$ Å); and "3" notates γ-MnO_2 (JCPDS No. 14−0644, orthorhombic, $a = 6.36$ Å, $b = 10.15$ Å, $c = 4.09$ Å).

3. RESULTS AND DISCUSSION

3.1. Physicochemical Characterizations. *3.1.1. XRD.* The XRD patterns of the prepared An-MnO_x and Py-MnO_x are shown in Figure 2. Both the patterns displayed low-intensity and broad peaks, indicating the small particle sizes and low crystallinities of the samples. The pattern of the An-MnO_x sample was lack of characteristic peaks, except for the small one at about 36°, indicating the sample to be amorphous in accordance with a previous study.[30] Whereas the Py-MnO_x sample exhibited small but noticeable characteristic peaks belonging to λ-MnO_2, α-MnO_2, and γ-MnO_2, showing higher crystallinity than the An-MO_x sample. Note that the 36° peak on the pattern of An-MnO_x is also present on that of Py-MnO_x, and can be assigned to α-MnO_2. Nevertheless, both samples prepared via interfacial synthesis contained mixed Mn valences and were of relatively low crystallinity. These features determined inherently the low signal/noise ratio on the XRD patterns, and the difficulty in full revelation of the crystalline phases. For the same reason, attempts failed to calculate the crystal sizes from the diffraction peaks using the Scherrer equation.

3.1.2. XPS. It was suggested that the surface properties of MnO_x, particularly the surface oxidation state and chemical composition, could impose significant influences on electrochemical capacitance which should be relevant to surface adsorption/desorption of ions and/or redox reactions within the oxide.[13,19,20] The surface oxidation states of the prepared samples were then studied by XPS.[3,41] As shown by the XPS in Figure 3A, B, manganese, oxygen, and trace potassium were the elements present in both the An-MnO_x and Py-MnO_x samples while nitrogen was absent, indicating the absence of polymers and oligomers. The presence of potassium in the MnO_x samples is understandable. In general, manganese oxides can form many polymorphs by interlinking the basic $[MnO_6]$ octahedra in different configurations. Some manganese oxide contains interlayer space or tunnels and some cations such as K^+ could be introduced during the synthesis process. However, the mass content of potassium is less than 3% on the basis of EDS tests. Therefore, the influence of potassium is negligible when fitting the XPS. The absence of nitrogen species was also evidenced by the CHNS-O analysis. As listed in Table 1, only a negligible amount of nitrogen was detected. The presence of small amounts of carbon can be derived from the remaining trace organic species. It was reported that both Mn 3s and Mn 2p XPS could be employed to indentify the oxidation state of Mn.[3,41] In this work, the Mn 2p XPS with a resolution of 0.1 eV was used to determine the surface Mn oxidation states. It can be seen from the Mn 2p XPS in Figure 3C,D that the surface of An-MnO_x was mainly consisted of Mn (III) species with less Mn (II) and least Mn (IV), whereas the dominant surface oxidation state of the Py-MnO_x was Mn (IV) with minor Mn(III). The water content of MnO_x is believed to be relevant to their electronic and ionic conductivities and thus related to their electrochemical properties.[42] The corresponding water contents of the two samples were then studied by O 1s XPS. As shown in Figure 3E,F, the O 1s XPS were composed of three parts of characteristic oxygen bonds: chemically bonded water (H−O−H), hydroxide (Mn−O−H) and oxide (Mn−O−Mn).[3] The higher contents of H−O−H and Mn−O−H presented in the Py-MnO_x sample indicate more chemically bonded water in the lattices of the sample.

It is worth mentioning that both the XPS and the XRD analyses indicated the products from the interfacial synthesis were dominantly composed of Mn and O. However, because partial valence variation of the Mn atom in the sample may not cause a significant change in the crystal structure, the XRD patterns may retain the same diffraction peaks. On the other hand, XPS is capable of detecting the Mn valence only on the sample's surface, while XRD provides more bulk information. Thus, these two techniques may provide different but complementary information of the same sample such as the MnO_x products from interfacial synthesis that contained mixed Mn valences.

3.1.3. TGA/DTA. The thermal properties of the samples were studied by TGA/DTA with typical results shown in Figure 4. The weight loss from room temperature to 100 °C can be attributed to the removal of physically adsorbed water in the samples, which accounts for the endothermic peaks at around 60 °C on both DTA curves. The weight loss near 200 °C can be assigned to the loss of chemically bonded water in the samples, which results in the formation of exothermic peaks at 190 °C on the DTA curves.[32,33,38] The exothermic DTA peak at 190 °C for the An-MnO_x sample was quite small, indicating the content of chemically bonded water in the sample was much lower. Note that the difference in water content between An-MnO_x and Py-MnO_x as revealed by XPS is much smaller than that shown by the DTA results. This again may be explained by XPS being surface-sensitive while DTA measures the bulk property.

The appearance of the exothermic peaks around 480 °C on both DTA curves is due to the oxygen adsorption, which should have slightly increased the weights.[32] However, the weights near 480 °C on both TGA curves were quite stable, which is due to the influence of the decomposition of MnO_2 to O_2 and Mn_2O_3.[35,38] The weight increase derived from the oxygen adsorption is largely balanced by the weight loss originated from the decomposition of MnO_2 to Mn_2O_3. As evidenced on the TGA curves, the weight loss between 550 and 600 °C for the Py-MnO_x sample can be attributed to the dominance of the decomposition of MnO_2 to Mn_2O_3, indicating the content of MnO_2 in the sample was higher. The results from XRD, XPS and TGA for the two samples are quite consistent. It can then be concluded that the Py-MnO_x sample had a higher content of Mn (IV) species and chemically bonded water. The morphology of the generated

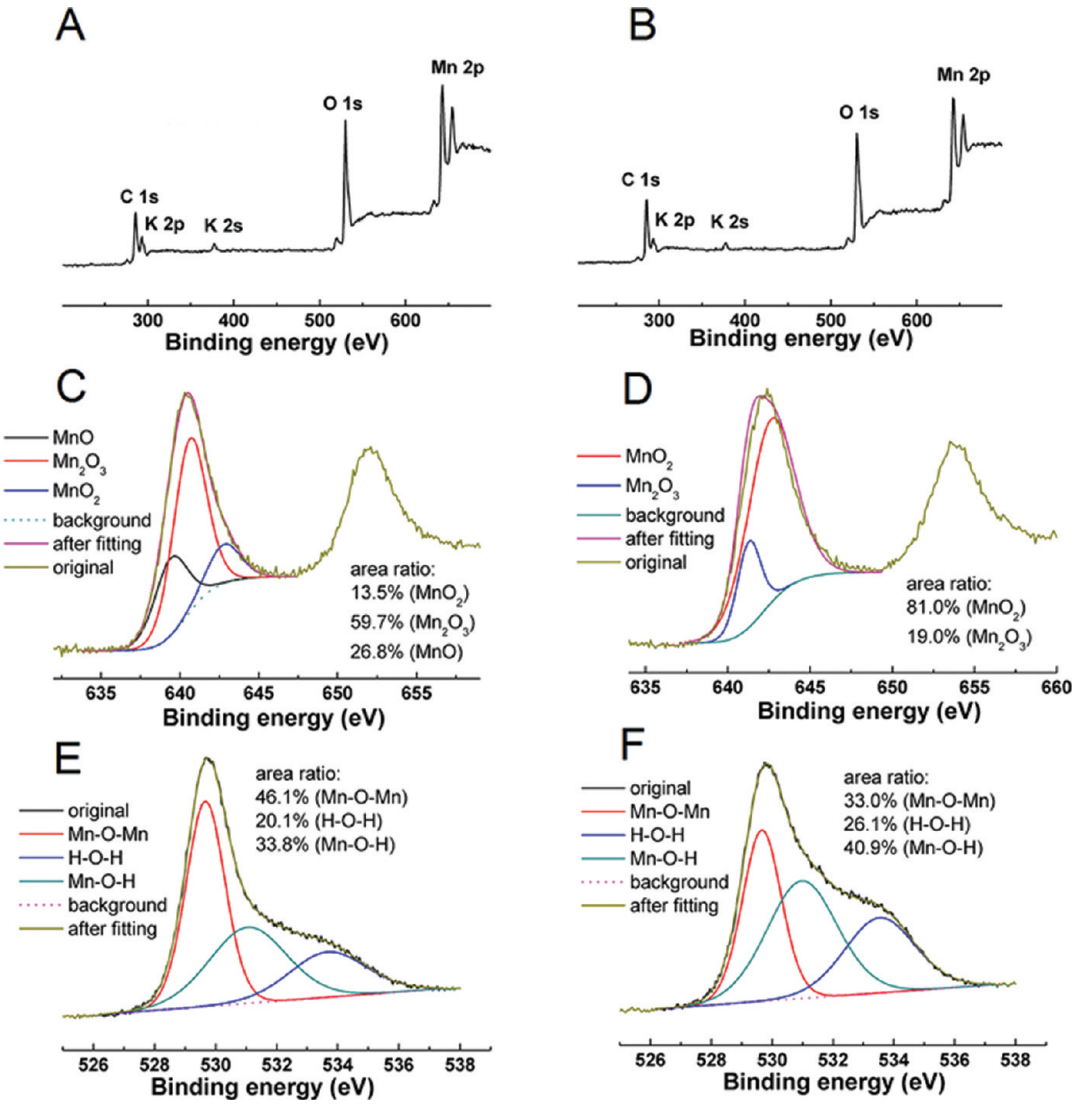

Figure 3. XPS spectra of the (A, C, E) An-MnO_x and (B, D, F) Py-MnO_x samples in (A, B) full, (C, D) Mn 2p and (E, F) O 1s regions. Note that besides the original spectrum, each panel contains the fitted spectrum, which was resolved into individual ones for each oxidation state.

Table 1. Elemental Compositions of Different MnO_x Samples Prepared in This Work

	nitrogen (wt %)	carbon (wt %)	hydrogen (wt %)	sulfur (wt %)
An-MnO_x[a]	0.07	0.58	2.33	0.00
Py-MnO_x[a]	0.06	0.56	2.17	0.00
P*o*AP/MnO_x[b]	1.58	9.74	1.36	0.00

[a] Prepared by interfacial synthesis. [b] Prepared by coprecipitation.

MnO_x was found to transfer into larger nanorods after annealing in air at 400 °C for 1 h (see Figure S2 in the Supporting Information).

3.1.4. SEM/HRTEM/SAED. The morphologies of the Py-MnO_x and An-MnO_x samples were studied by SEM and TEM. In the SEM images of Figure 5A,B, both samples exhibited porous microstructures formed by three-dimensionally (3D) interconnected uniform NPs in pseudospherical shapes. The sizes of the NPs ranged from 10 to 15 nm for An-MnO_x and from 15 to 20 nm for Py-MnO_x, respectively. The corresponding HRTEM images presented in Figure 5C,D show clearly that the NPs had a hierarchical microstructure in which the pseudospherical nanoparticles were composed of interconnected finer NPs of varying sizes less than 5 nm. As evidenced by the insets of Figure 5, the SAED patterns of the samples were generally blurred, revealing low crystallinity. The SEAD patterns also indicated that Py-MnO_x was slightly higher in crystallinity than An-MnO_x. Thus, the SEAD analysis is in well agreement with the corresponding XRD analysis. In line with XRD and SEAD analyses, it was found from the HRTEM that the lattice fringes were overlapped, preventing a satisfactory resolution for deriving the *d*-spacing values, which can be ascribed to the low crystallinity and mixed valences of the prepared samples. The HRTEM images also suggested the ultrafine NPs to be interconnected into a network in which nanopores were present.

3.1.5. BET. The nanoporous features of the two samples were then verified by the N_2 adsorption/desorption isotherms. In Figure 6A, the isotherms of the two samples exhibited a typical

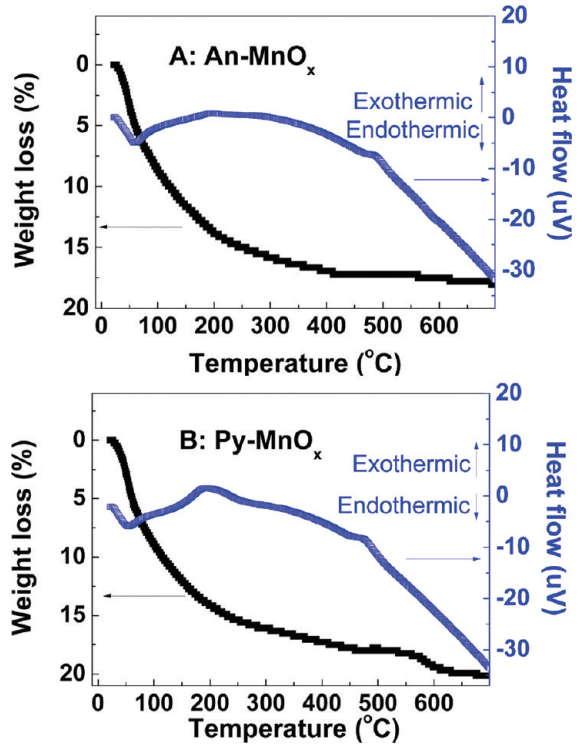

Figure 4. TGA/DTA curves of the (A) An-MnO_x and (B) Py-MnO_x samples.

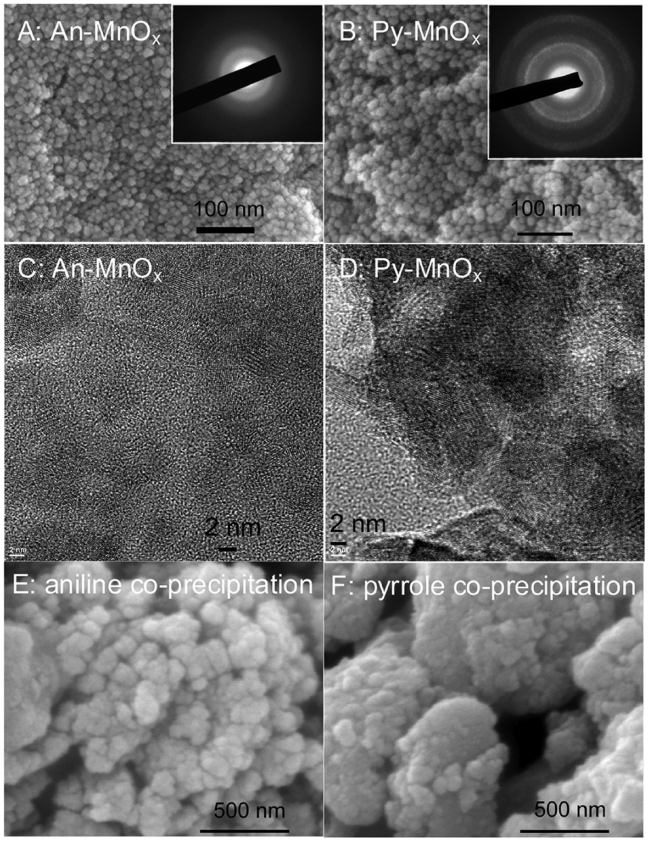

Figure 5. Typical (A, B, E, F) FESEM and (C, D) HRTEM images of the samples prepared via (A–D) interfacial synthesis and (E, F) coprecipitation synthesis using aniline (A, C, E) and pyrrole (B, D, F) as the precursory monomer. The insets display the corresponding SAED patterns.

type IV isotherm with a type H2 of hysteresis loop, suggesting mesoporous structures.[43] The BET surface areas and pore volumes of the two samples are summarized in Table 2. The specific surface areas were estimated to be as high as 151.5 and 128.3 $cm^2\ g^{-1}$ for An-MnO_x and Py-MnO_x, respectively. In detail, the isotherm of An-MnO_x gave a hysteresis loop in the relative pressure range of 0.50–0.80 and a plateau in the higher relative pressure range. For Py-MnO_x, the hysteresis loop on the isotherm shifted to a higher relative pressure range (0.50–0.90) and only a pseudoplateau appeared on the isotherm. These are indicative of the presence of larger mesopores in the Py-MnO_x sample.[33] In Figure 6B, the pore size distribution (PSD) in the An-MnO_x sample was centered in a narrow range between 3.0 and 8.2 nm, while in Py- MnO_x between 3.8 and 9.8 nm. The narrow PSDs indicate that the generated mesoporous matrixes were derived from the aggregation or compaction of the ultrafine nanoparticulate building blocks.[43] The pore volumes were calculated to be 0.256 and 0.185 $cm^3\ g^{-1}$ for An-MnO_x and Py-MnO_x, respectively.

3.2. Interfacial Reaction Mechanisms. It has been demonstrated that the building blocks of the prepared An-MnO_x and Py-MnO_x are of ultrafine nanoparticles with diameters less than 5 nm, which highlights the merits of the interfacial synthesis on retarding the growth of nuclei. It was recently reported that the MnO_x-based products prepared via the interfacial synthesis utilizing thiophene or 3,4-ethylenedioxythiophene (EDOT) as precursory monomers were composed of the building blocks of ultrathin nanosheets thinner than 10 nm.[9,37,38] The anomalous interfacial properties are believed to be relevant to the formation of ultrafine/ultrathin building blocks in the interfacial synthesis.[30] In the interfacial synthesis, the nuclei formation, growth and aggregation processes are confined to occurring near the interface where the extremely high interfacial tensions exist. The Ostwald ripening is restrained under the influence of the anomalous interfacial forces. In the absence of the interfacial influences, the MnO_x prepared via the coprecipitation route were much larger particles with lower porosity, as depicted in Figure 5E and 5F.

The generated ultrathin/ultrafine building blocks then assemble or aggregate, in order to minimize the surface energy. The morphology and chemical composition of the final products are found to be related with the precursory monomers. When using thiophene or EDOT as the feedstock, the final products were polymer/MnO_x composites composed of submicro-spheres assembled from ultrathin nanosheets.[9,37,38] However, pseudospherical MnO_x NPs with diameters less than 20 nm aggregated from ultrafine NPs smaller than 5 nm were formed when using aniline or pyrrole as the feedstock. It is shown that aniline or pyrrole is more effective on constraining the assembly or aggregation of the building blocks. The mechanism of interfacial synthesis was discussed previously.[38] However, the significant differences in morphology and compositions of the products using different monomers stimulate further consideration of the formation mechanism, especially in terms of the roles of the precursory monomers.

In the interfacial synthesis, the redox reaction between monomers and MnO_4^- is confined near the interface, resulting in the formation of MnO_x nuclei and monomeric radical cations near

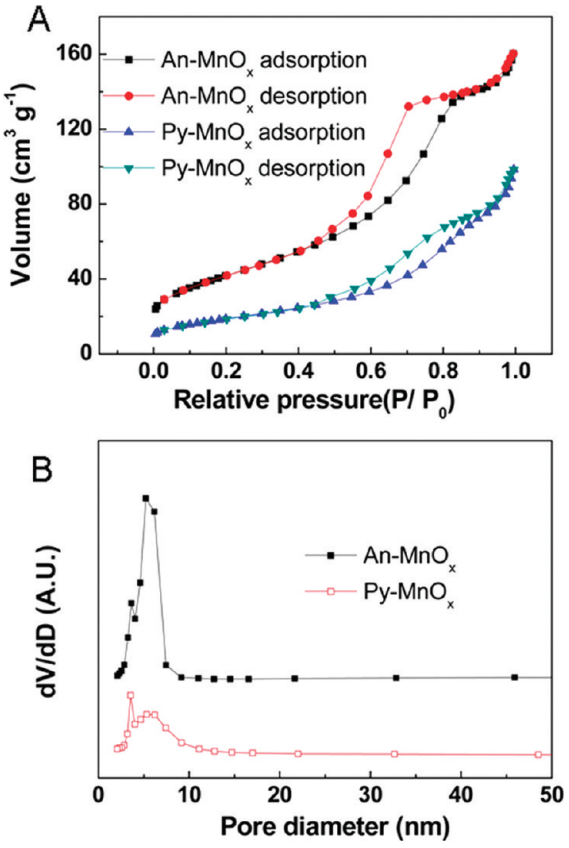

Figure 6. (A)N_2 adsorption−desorption isotherms and (B) pore-size distributions of the MnO_x samples prepared by interfacial synthesis.

Table 2. Specific Surface Areas and Pore-Size Distributions Derived from the N_2 Adsorption−Desorption Isotherms of the Samples Prepared by Interfacial Synthesis

	An-MnO_x	Py-MnO_x
specific surface area (cm^2 g^{-1})	151.4	128.3
pore volume (cm^3 g^{-1})	0.256	0.185

the interface. The generated nuclei should exist in the aqueous phase near the interface since MnO_x are hydrophilic. The generated monomeric radical cations have extremely high reactivity and can spontaneously couple together or couple with other monomers to form oligomers or polymer.[38,44] Polymer chain propagation, as a redox reaction between growing chains and monomers, will take place if their oxidation potentials are equilibrated.[44] Aniline and pyrrole can dissolve well in aqueous solutions whereas thiophene or EDOT are scarcely soluble in water.[45] Therefore, aniline or pyrrole can diffuse between the organic and aqueous phases, leading to the change of the chemical potentials of aniline or pyrrole near the interface. As a result, the propagation of polyaniline or polypyrrole chains terminates soon, leading to the formation of short-chain oligomers. The generated oligomers which are more hydrophobic than the monomers then diffuse into the organic phase. It is shown in Figure 1 that the organic phase became yellow after reaction, indicating the presence of dissolved oligomers. During reaction, thiophene or EDOT can hardly transfer between the organic and aqueous phases, incurring a consistent equilibration

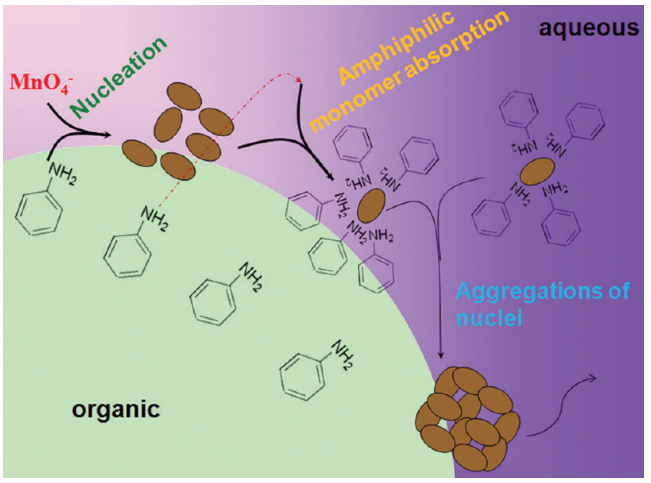

Figure 7. Schematic representation of the aniline-assisted interfacial synthesis of mesoporous MnO_x nanoparticles.

in chemical potential of monomers and growing chains.[44] In this case, the chain propagation is prolonged, which facilitates the formation of longer chain polymers instead of oligomers. The generated polymers are then attached to the MnO_x and results in the formation of MnO_x/polymer composites.

In general, interfacial synthesis produces nanoscale building blocks that have high tendency to assemble or aggregate to reduce surface energy. When using thiophene or EDOT as the precursory monomer, the assembly of building blocks (ultrathin nanosheets) is not effectively controlled, although the generated polymers can cap on the surface of the building blocks, resulting in the formation of submicrometer-spheres.[9,37,38] When using aniline or pyrrole as the precursory monomer, the excess monomers can pass through the interface and diffuse into the aqueous phase near the interface where the monomers can absorb onto the building blocks, resulting in the formation of nuclei-monomer micelles in the aqueous phase near the interface. Thus, the absorbed monomers function as an effective structure directing agent capable of retarding the aggregation of the build blocks, resulting in the formation of pseudospherical MnO_x NPs (<20 nm) that can well-disperse in the aqueous phase due to their hydrophilic nature (see Figure 1). The formation mechanism of the interfacial synthesis using aniline or pyrrole as precursory monomers (namely monomer-assisted synthesis) is schematically illustrated in Figure 7 with the aniline-assisted synthesis as an example. It should be noted that the pore properties of the MnO_x NPs prepared by interfacial synthesis were different, although the samples generally showed typical mesoporous features with type IV isotherms. It was reported that the generated PEDOT/MnO_x nanocomposite displayed a hysteresis loop of type H3, in which the mesopores arose from the packing of ultrathin nanosheets.[37] It was different for the generated An-MnO_x and Py-MnO_x which showed hysteresis loops of type H2, suggesting interstitial pores between adjacent building blocks (<5 nm) and the voids in the 3D interconnected network. The formed mesopores are believed to be relevant to the steric effects during the aggregation process.

The importance of the amphiphilicity of the precursory monomers was further validated by the experimental results from synthesizing the P*o*AP/MnO_x composite *via* the coprecipitation method. The monomer, *o*AP, is a solid with a low

solubility in water. The elemental analysis (summarized in Table 1) of the PoAP/MnO_x composite sample revealed the presence of nitrogen and carbon with a molar ratio of N/C very close to that in PoAP, indicating the formation of polymer. The SEM images of the sample presented in Figure 8A and 8B display the microscale MnO_x matrix in which PoAP nanobelts were embedded. It can also be noticed that the MnO_x blocks are very dense, indicating the occurrence of significant nuclei aggregation. With low solubility in aqueous solutions, the monomer *o*AP has no effect on the nuclei formation and building block aggregations, leading to the formation of microscale MnO_x matrixes. In addition, the chemical potential of dissolved *o*AP should be constant during the homogeneous reaction, sustaining polymer chain propagation to the formation of the PoAP/MnO_x composite. Interestingly, it was observed that the embedded PoAP nanobelts were unstable. Upon exposure to a strong electron beam irradiation in vacuum for 3 h in the first day, the number and lengths of PoAP nanobelts decreased noticeably (see Figure 8C). When repeating the irradiation for additional 3 h in the second day, the nanobelts almost disappeared, leaving a dense coating of PoAP on the MnO_x clusters (see Figure 8D). PoAP was reported to possess promising electrochemical properties despite its low conductivity.[46] The generated PoAP/MnO_x composite is expected to be useful electrode materials for electrochemical devices. The investigation of its electrochemical properties is still ongoing.

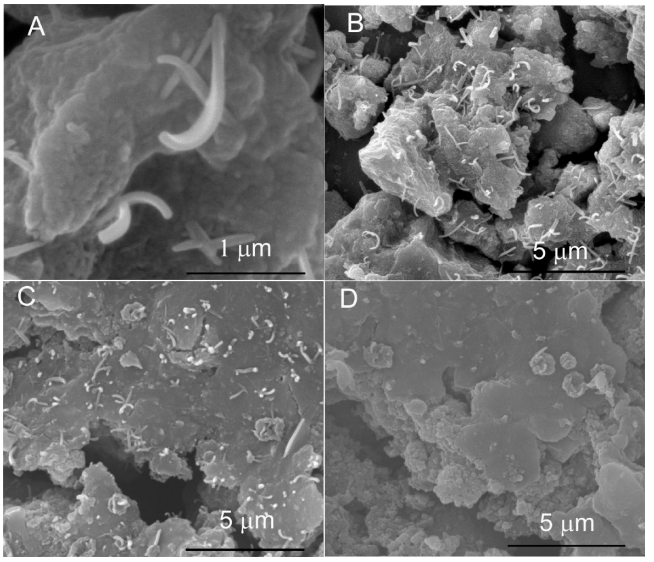

Figure 8. SEM images of the sample prepared via the coprecipitation reaction between $KMnO_4$ and *o*-aminophenol (A, B) without or with exposure to electron beam irradiation for (C) 3 h in the first day, and (D) additional 3 h in the second day at an accelerated voltage of 30 kV in vacuum.

3.3. Electrochemical Capacitance. The electrochemical properties of the prepared An-MnO_x and Py-MnO_x electrodes were studied by CV and GCD in aqueous Na_2SO_4 solutions. The corresponding CVs and GCDs are shown in Figure 9. The CVs generally showed rectangular features with no obvious redox

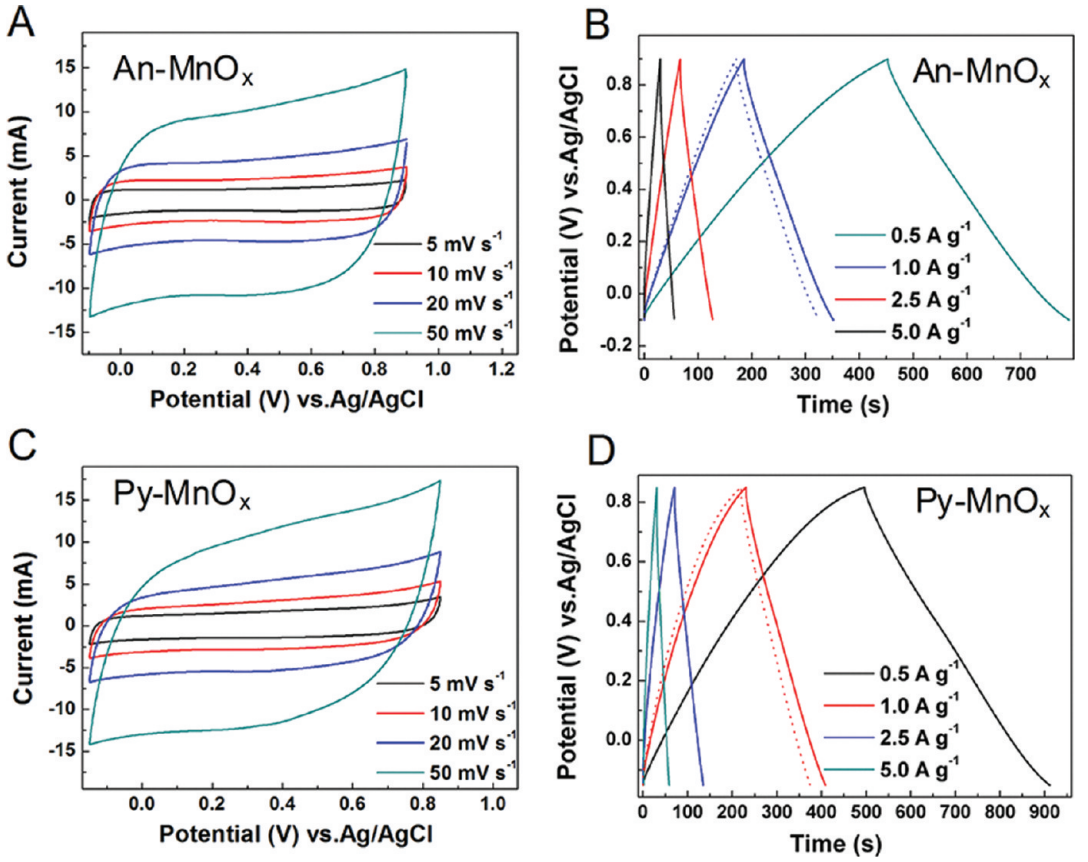

Figure 9. (A, C) CV and (B, D) GCD plots of the (A, B) An-MnO_x and (C, D) Py-MnO_x electrodes in 1.0 M Na_2SO_4 solution. The dashed plots in B and D display the corresponding GCD plots after 1000 consecutive cycles at a normalized charge/discharge current of 1 A g^{-1}.

Table 3. Specific Capacitance Values of the Samples Prepared by Interfacial Synthesis[c]

specific capacitance (F g^{-1}, CVs)			specific capacitance (F g^{-1}, GCDs)		
scan rate (mV s^{-1})	An-MnO_x	Py-MnO_x	norm. current (A g^{-1})	An-MnO_x	Py-MnO_x
5	160.4	194.0	0.5	197.6	227.8
10	147.5	188.1	1.0	175.8	205.9
20	138.6	174.3	2.5	160.6	169.5
50	122.5	150.6	5.0	140.7	146.3

[c] The listed specific capacitance (F g^{-1}) can be converted to electrode geometry normalized capacitance (F cm^{-2}) using the loadings of 1.50 and 1.41 mg cm^{-2} for An-MnO_x and Py-MnO_x, respectively (see Experimental Section). For example, at 0.5 A g^{-1}, the electrode capacitance can be calculated to be 1.41 × 227.8/1000 = 0.321 F cm^{-2} for Py-MnO_x, and 1.50 × 197.6/1000 = 0.296 F cm^{-2} for An-MnO_x

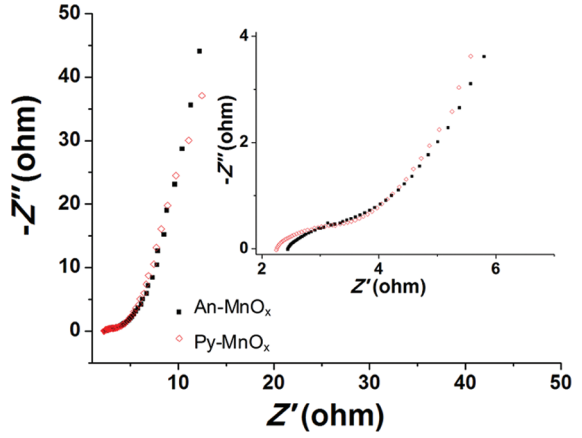

Figure 10. Nyquist plots for An-MnO_x and Py-MnO_x electrodes in 1.0 mol L^{-1} Na_2SO_4 solution. The inset displays the enlarged high frequency portions of the plots.

peaks in the working potential window of 1.0 V. All presented GCDs exhibit that the potential varies linearly with time during charging and discharging. Both the CV and GCD results indicate the nearly ideal capacitive properties of the prepared An-MnO_x and Py-MnO_x electrodes. The calculated specific capacitances are summarized in Table 3, falling between 122.5 and 227.8 F g^{-1}. These values are comparable to those previously reported for the 3D frameworks of homogeneous MnO_x NPs of 5 nm in size.[33] It is worth noting that at the Py-MnO_x loading of 1.41 mg cm^{-2}, the capacitance normalized to the electrode's geometric area was 0.321 F cm^{-2}. A linear projection could then reach 5 F cm^{-2} at 22 mg cm^{-2}. This is very promising considering a recent report of 5 F cm^{-2} at 35 mg cm^{-2} for composites of MnO_x and carbon nanotubes,[17] and calls for further studies on, for example, materials improvement and electrode design.

The prepared MnO_x electrodes were also characterized by EISs. The Nyquist plots of both Py-MnO_x and An-MnO_x in Figure 10 are dominated by a tilted vertical line at low frequencies, which is characteristic of capacitive behavior.[20,38] The Py-MnO_x sample had a noticeably shorter capacitive line than An-MnO_x, and hence higher capacitance. At high frequencies, a very small but depressed semicircle appeared on both plots, indicating easy kinetics for charge transfer through the interface.[38] The Py-MnO_x electrode also showed a smaller resistance than the An-MnO_x electrode as evidenced by the high frequency intercepts with the Z′ axis. Thus, the EIS findings agree well with those of CVs and GCDs, verifying Py-MnO_x and An-MnO_x as highly capacitive materials with Py-MnO_x being possibly a preferred choice. More EIS details are presented in Figure S3 in the Supporting Information.

The stability of the prepared MnO_x electrodes was studied by consecutive 1000 cycles of GCD at a normalized current of 1 A g^{-1}. The corresponding GCD plots after cycling are superimposed in Figure 9B,D (dashed lines), confirming the An-MnO_x and Py-MnO_x electrodes to have retained 91.4% and 92.4% of their initial capacitances, respectively. During the charge/discharge processes, MnO_x experienced multiple redox reactions with changes in valence. Some solid MnO_x may be electroreduced to soluble species, e.g. the Mn^{2+} ion, but only part of the dissolved species could be electro-recovered to solid MnO_x.[18,38] Such a dissolution-deposition process incurs progressive loss of activities of the MnO_x electrodes. The presence of soluble manganese species such as Mn^{2+} in the electrolyte was qualitatively identified by the following experiment. After 1000 charge/discharge cycles on the An-MnO_x electrode, a small amount of sodium periodate was added into the electrolyte which then became pink (see Figure S4 in the Supporting Information). It is known that Mn^{2+} can be oxidized to MnO_4^- by periodate. Thus the observed color change in the electrolyte indicates the conversion of Mn^{2+} to MnO_4^- ions, which in turn validates the dissolution-deposition mechanism being at least partially responsible for the capacitance fade in manganese oxides. In addition, the redox reactions in the MnO_x electrodes are accompanied by volume changes resulting from the uptake/extraction of cations. The local stresses originated from volume changes may cause failures of the electrodes.[18,38] The microstructures of the prepared MnO_x electrodes after cycling were found to be changed. As shown in Figure 11, upon long-time cycling, the grain sizes increased and the interconnections between individual nanoparticles partially disappeared. The average grain size of An-MnO_x changed from less than 15 nm to a range between 15 and 20 nm, while that of Py-MnO_x increased from less than 20 nm to a range between 20 and 25 nm. Such grain growth can obviously contribute to the performance decay of the MnO_x under continuous charge/discharge cycling. It was reported that nanopainting the pristine MnO_x with conducting polymers could be an effective approach to enhancing their stabilities and cycling performances.[38]

The good capacitive properties of the prepared An-MnO_x and Py-MnO_x electrodes can be attributed to their microstructures. The resulting ultrafine NPs with high specific surface areas can lower charge transfer barriers and shorten solid-state transport lengths.[36] The 3D interconnected features facilitate electron transfers through the whole electrodes.[33] The open porous matrixes will allow faster diffusion of electrolytes.[36]

It is acknowledged that the MnO_x electrodes were fabricated with added carbon and binder which may influence the electrochemistry of MnO_x. However, because MnO_x was the dominant component of the electrode materials, it should have been the determining factor on the electrode performance. Another concern is the influence of the electrode fabrication procedures (such as blending, grinding and pressing) on the structure of the MnO_x NPs. This is thought to be insignificant because the pores

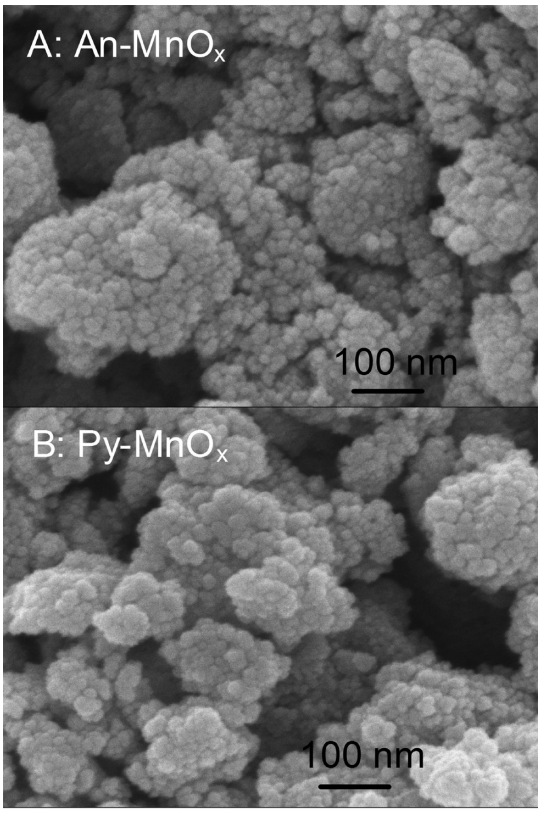

Figure 11. Typical FESEM images of the (A) prepared An-MnO_x and (B) Py-MnO_x electrodes after 1000 consecutive GCD cycles at a normalized current of 1 A g^{-1}. Before SEM measurements, the electrodes were fully rinsed in *N*-methyl-2-pyrrolidone to remove the binder.

and particles were too small to be accessed by manual operations. In addition, the fabrication procedure was deliberately kept the same, which makes it reasonable to compare the difference in performance on the basis of the content and properties of MnO_x in the electrode.

The first interesting observation was that although the An-MnO_x sample possessed a higher BET surface area and lower average Mn valence (close to III) on the surface than the Py-MnO_x sample, the latter conveyed higher specific capacitance. This finding is indicative of the surface conditions and double-layer storage mechanism to be nonpredominant. It was demonstrated that the charge storage mechanism of MnO_x electrodes is mainly faradic.[47] Therefore, the differences in capacitance between An-MnO_x and Py-MnO_x can be attributed to their dissimilar bulk properties, rather than the surface conditions. As for the higher average Mn valence on the surface of Py-MnO_x, this should have had little influence because the charge transfer reaction, which makes conversion between different Mn oxidation states, was very fast and reversible.

The crystallographic properties of MnO_x were found to be significantly relevant to their capacitances.[47,48] It was reported that the capacitances of MnO_x decreased linearly with decreasing crystallinity due to the lower conductivity of less crystalline MnO_x.[49] The XRD results suggest Py-MnO_x was of higher crystallinity than An-MnO_x. The crystalline MnO_x with suitable tunneled or interlayered structures are more favorable for accommodating and transporting cations.[33,47,48] The α- and λ-MnO_2 phases as detected by XRD in the prepared Py-MnO_x are known to possess molecular level 3D and 1D cation conduction channels and hence relatively high ionic conductivity.[47] Easy conduction of cations throughout the bulk of MnO_x is needed for Faradic reactions to proceed to completion, and accounts for the reported correlation between the specific capacitance and the ionic conductivity of MnO_x powders.[47] Hydrate contents are also known to influence the ionic conductivities.[42] A high water content is believed to be beneficial to the proton hopping process.[50] The Py-MnO_x sample had a higher water content and hence greater proton conductivity than the An-MnO_x sample. Therefore, the difference in capacitance between An-MnO_x and Py-MnO_x should have been more related to their crystallographic properties and water contents than to their surface areas.

4. CONCLUSIONS

Mesoporous manganese oxide (MnO_x) matrixes consisting of three-dimensionally interconnected and uniform pseudospherical nanoparticles (NPs) with diameters less than 20 nm have been successfully synthesized by using aniline or pyrrole to reduce MnO_4^- ions at the CH_2Cl_2/H_2O interface. Both pyrrole and aniline are amphiphilic and can therefore pass through the organoaqueous interface into the aqueous phase, leading to adsorption on the MnO_x nuclei. The adsorbed monomers function as effective structure directing agents capable of retarding the aggregation of the MnO_x nuclei, resulting in the formation of ultrafine MnO_x NPs. The amphiphilic monomers were also found to avoid polymerization in the presence of the MnO_x NP at the organoaqueous interface.

The importance of the solubility of the precursory monomer in the aqueous phase was further verified by replacing aniline or pyrrole with the more hydrophobic *o*-aminophenol (*o*AP) in similar experiments. The produced P*o*AP/MnO_x composite was composed of microscale MnO_x blocks in which P*o*AP nanobelts were embedded.

The An-MnO_x and Py-MnO_x NPs prepared by interfacial synthesis possessed high surface areas and open mesoporous structure as revealed by BET, SEM and HRTEM. CVs and GCDs confirmed the prepared MnO_x NPs to be highly capacitive in the potential window of 0−0.9 V vs Ag/AgCl, promising their use as positive electrode materials in supercapacitors. The specific capacitance as measured by CVs and GCDs ranged from 122.5 to 227.8 F g^{-1}. At a Py-MnO_x loading of 1.41 mg cm^{-2}, the capacitance normalized to the electrode's geometric area reached beyond 0.3 F cm^{-2}. It was also found that although the synthesized An-MnO_x had a higher specific surface area than Py-MnO_x, the latter exhibited higher specific capacitance. This can be ascribed to Py-MnO_x having greater crystallinity for better electron conduction (according to XRD and EIS, respectively), and higher water content (from TGA/DST and XPS analyses) and more molecular level channels (in the XRD identified α- and λ-MnO_2 phases) for easy transfer of cations within the material.

■ ASSOCIATED CONTENT

Supporting Information. Figures S1, S2, S3, and S4 as stated in the paper (PDF). This information is available free of charge via the Internet at http://pubs.acs.org/

AUTHOR INFORMATION

Corresponding Author

*Tel.: +44 115 951 4171. Fax: +44 115 951 4115. E-mail: george.chen@nottingham.ac.uk (G.Z.C).

ACKNOWLEDGMENT

We thank E.ON AG for funding through the E.ON International Research Initiative – Energy Storage 2007. W. X. did some verification experiments using a start-up grant from Wuhan University. Responsibility for the content of this paper lies with the authors.

REFERENCES

(1) Brock, S. L.; Duan, N. G.; Tian, Z. R.; Giraldo, O.; Zhou, H.; Suib, S. L. *Chem. Mater.* **1998**, *10*, 2619–2628.
(2) Xiao, W.; Xia, H.; Fuh, J. Y. H.; Lu, L. *J. Electrochem. Soc.* **2009**, *156* (7), A627–A633.
(3) Chigane, M.; Ishikawa, M. *J. Electrochem. Soc.* **2000**, *147* (6), 2246–2251.
(4) Chabre, Y.; Pannetier, J. *Prog. Solid State Chem.* **1995**, *23* (1), 1–130.
(5) Yao, S. J.; Xu, J. H.; Wang, Y.; Chen, X. X.; Xu, Y. X.; Hu, S. S. *Anal. Chim. Acta* **2006**, *557* (1–2), 78–84.
(6) Bai, Y. H.; Du, Y.; Xu, J. J.; Chen, H. Y. *Electrochem. Commun.* **2007**, *9* (10), 2611–2616.
(7) Thackeray, M. M.; Rossouw, M. H.; Dekock, A.; Delaharpe, A. P.; Gummow, R. J.; Pearce, K.; Liles, D. C. *J. Power Sources* **1993**, *43* (1–3), 289–300.
(8) Wu, M. S.; Chiang, P. C. J.; Lee, J. T.; Lin, J. C. *J. Phys. Chem. B* **2005**, *109* (49), 23279–23284.
(9) Xiao, W.; Chen, J. S.; Lu, Q.; Lou, X. W. *J. Phys. Chem. C* **2010**, *114* (27), 12048–12051.
(10) Cheng, F. Y.; Su, Y.; Liang, J.; Tao, Z. L.; Chen, J. *Chem. Mater.* **2010**, *22* (3), 898–905.
(11) Xiao, W.; Wang, D. L.; Lou, X. W. *J. Phys. Chem. C* **2010**, *114* (3), 1694–1700.
(12) Cheng, F. Y.; Shen, J.; Ji, W. Q.; Tao, Z. L.; Chen, J. *ACS Appl. Mater. Interfaces* **2009**, *1* (2), 460–466.
(13) Wei, W. F.; Cui, X. W.; Chen, W. X.; Ivey, D. G. *Chem. Soc. Rev.* **2011**, *40* (3), 1697–1721.
(14) Xia, H.; Lai, M. O.; Lu, L. *JOM* **2011**, *63* (1), 54–59.
(15) Hu, C. C.; Tsou, T. W. *Electrochem. Commun.* **2002**, *4* (2), 105–109.
(16) Toupin, M.; Brousse, T.; Belanger, D. *Chem. Mater.* **2002**, *14* (9), 3946–3952.
(17) Jin, X. B.; Zhou, W. Z.; Zhang, S. W.; Chen, G. Z. *Small* **2007**, *3* (9), 1513–1517.
(18) Zhang, S. W.; Peng, C.; Ng, K. C.; Chen, G. Z. *Electrochim. Acta* **2010**, *55* (25), 7447–7453.
(19) Chae, J. H.; Ng, K. C.; Chen, G. Z. *Proc. Inst. Mech. Eng., Part A: J. Power Energy* **2010**, *224* (A4), 479–503.
(20) Zhang, S. W.; Chen, G. Z. *Energy Mater.* **2008**, *3* (3), 186–200.
(21) Simon, P.; Gogotsi, Y. *Nat. Mater.* **2008**, *7* (11), 845–854.
(22) Arico, A. S.; Bruce, P.; Scrosati, B.; Tarascon, J.-M.; van Schalkwijk, W. *Nat. Mater.* **2005**, *4* (5), 366–377.
(23) Broughton, J. N.; Brett, M. J. *Electrochim. Acta* **2005**, *50* (24), 4814–4819.
(24) Nagarajan, N.; Humadi, H.; Zhitomirsky, I. *Electrochim. Acta* **2006**, *51* (15), 3039–3045.
(25) Wang, X.; Li, Y. D. *Chem.—Eur. J.* **2003**, *9* (1), 300–306.
(26) Xu, M.; Kong, L.; Zhou, W.; Li, H. *J. Phys. Chem. C* **2007**, *111* (51), 19141–19147.
(27) Zhu, H. T.; Luo, J.; Yang, H. X.; Liang, J. K.; Rao, G. H.; Li, J. B.; Du, Z. M. *J. Phys. Chem. C* **2008**, *112* (44), 17089–17094.
(28) Luo, J.; Zhu, H. T.; Fan, H. M.; Liang, J. K.; Shi, H. L.; Rao, G. H.; Li, J. B.; Du, Z. M.; Shen, Z. X. *J. Phys. Chem. C* **2008**, *112* (33), 12594–12598.
(29) Voorhees, P. W. *J. Stat. Phys.* **1985**, *38* (1–2), 231–252.
(30) Yuan, J. K.; Laubernds, K.; Zhang, Q. H.; Suib, S. L. *J. Am. Chem. Soc.* **2003**, *125* (17), 4966–4967.
(31) Ni, J. P.; Lu, W. C.; Zhang, L. M.; Yue, B. H.; Shang, X. F.; Lv, Y. *J. Phys. Chem. C* **2009**, *113* (1), 54–60.
(32) Ragupathy, P.; Park, D. H.; Campet, G.; Vasan, H. N.; Hwang, S. J.; Choy, J. H.; Munichandraiah, N. *J. Phys. Chem. C* **2009**, *113* (15), 6303–6309.
(33) Wang, Y. T.; Lu, A. H.; Zhang, H. L.; Li, W. C. *J. Phys. Chem. C* **2011**, *115* (13), 5413–5421.
(34) Ragupathy, P.; Vasan, H. N.; Munichandraiah, N. *J. Electrochem. Soc.* **2008**, *155* (1), A34–A40.
(35) Reddy, R. N.; Reddy, R. G. *J. Power Sources* **2004**, *132* (1–2), 315–320.
(36) Wang, Y. G.; Wu, W.; Cheng, L.; He, P.; Wang, C. X.; Xia, Y. Y. *Adv. Mater.* **2008**, *20* (11), 2166–2170.
(37) Lu, Q.; Zhou, Y. K. *Funct. Mater. Lett.* **2011**, *4* (1), 31–36.
(38) Lu, Q.; Zhou, Y. K. *J. Power Sources* **2011**, *196* (8), 4088–4094.
(39) Yang, X. H.; Wang, Y. G.; Xiong, H. M.; Xia, Y. Y. *Electrochim. Acta* **2007**, *53* (2), 752–757.
(40) Yuan, C.; Gao, B.; Su, L.; Zhang, X. *J. Colloid Interface Sci.* **2008**, *322* (2), 545–550.
(41) Briggs, D.; Seah, M. P. *Practical Surface Analysis*, 2nd ed.; Wiley-Interscience: Chichester, U.K., 1990; Vol. 1.
(42) Rajendra Prasad, K.; Miura, N. *Electrochem. Commun.* **2004**, *6* (10), 1004–1008.
(43) Sing, K. S. W.; Everett, D. H.; Haul, R. A. W.; Moscou, L.; Pierotti, R. A.; Rouquerol, J.; Siemieniewska, T. *Pure Appl. Chem.* **1985**, *57*, 603–619.
(44) Gospodinova, N.; Terlemezyan, L. *Prog. Polym. Sci.* **1998**, *23* (8), 1443–1484.
(45) Peng, C.; Snook, G. A.; Fray, D. J.; Shaffer, M. S. P.; Chen, G. Z. *Chem. Commun.* **2006**, (44), 4629–4631.
(46) Hu, D.; Peng, C.; Chen, G. Z. *ACS Nano* **2010**, *4* (7), 4274–4282.
(47) Ghodbane, O.; Pascal, J. L.; Favier, F. D. R. *ACS Appl. Mater. Interfaces* **2009**, *1* (5), 1130–1139.
(48) Devaraj, S.; Munichandraiah, N. *J. Phys. Chem. C* **2008**, *112* (11), 4406–4417.
(49) Taguchi, A.; Inoue, S.; Akamaru, S.; Hara, M.; Watanabe, K.; Abe, T. *J. Alloys Compd.* **2006**, *414* (1–2), 137–141.
(50) McKeown, D. A.; Hagans, P. L.; Carette, L. P. L.; Russell, A. E.; Swider, K. E.; Rolison, D. R. *J. Phys. Chem. B* **1999**, *103* (23), 4825–4832.